Heliyon 10 (2024) e29792

Contents lists available at ScienceDirect

Heliyon

journal homepage: www.cell.com/heliyon

Research article

Photocatalytic activity and magnetic properties of Ba_2FeMoO_6 ferromagnetic double perovskite

Z. Ghorbani , M.H. Ehsani *

Faculty of Physics, Semnan University, PO Box: 35195-363, Semnan, Iran

ARTICLE INFO

Keywords:
Photocatalyst
Degradation
CTAB
Malachite green
Adsorption-desorption

ABSTRACT

Ba_2FeMoO_6 samples were prepared using the sol-gel method without and using Cetyltrimethylammonium bromide (CTAB) to study their photocatalytic properties. The structural and morphological properties of the samples were characterized systematically. The Rietveld refinement described a cubic structure with space group Fm-3m and a single phase with no detectable impurity for either. FESEM images showed that the sample's morphology changed significantly with the addition of the CTAB. The BET analysis of the sample containing CTAB (BFMOC) showed that the special surface area of the pores increased ten times compared to parent sample and its pore size decreased. The UV–Vis spectrum of the BFMOC sample showed two absorption peaks at 223 nm and 705 nm in the ultraviolet and visible regions, respectively. Diffuse reflectance spectroscopy (DRS) spectra of the samples showed direct band gaps (~2eV) for both. Photocatalytic and absorbent properties were observed in both samples. The photocatalytic properties of the samples revealed that they effectively degraded the dye triphenylmethane MG. By adding CTAB, the Curie temperature of the BFMO sample increased from 304 K to 310 K, while saturation magnetization decreased from ~1.43 μ_B/f.u to ~0.89 μ_B/f.u. The low coercive field value indicates that the both samples possess soft magnetic and ferromagnetic properties.

1. Introduction

The textile industry generates large amounts of waste-water, which has harmful effects and seriously threatens human health and the environment. Since some of these dyes are non-degradable, they can block sunlight and potentially stop the photosynthetic process [1]. In the past, most dyes used in industry were natural, i.e., derived from animals and plants. Synthetic dyes have been produced annually for several decades, and a large portion of these dyes is released into the environment [2].

The dye triphenylmethane, known as malachite green (MG), is used in the textile, paper, and leather industries [1]. Also, it is a therapeutic agent to treat and prevent fungal and parasitic infections [3] in fish. This toxic and poorly biodegradable compound cannot be removed from aqueous solutions using conventional methods.

Currently, many physical, chemical, biological, and electrochemical methods, such as adsorption and visible light degradation, are used to remove toxic dyes. These techniques have varying degrees of success [1,4]. Among all these methods, the adsorption method is one of the most suitable methods for absorbing organic pollutants from water because of its low cost, simple operation, environmental friendliness, and wide range of applications. Andrade et al. [1] used $H_2O_2/MnFe_2O_4$ to remove the MG dye from aqueous effluents in 60 min without changing the pH of the solution. Muinde et al. [4] reported that 1.2 g of CS–ZnO material removed malachite green

* Corresponding author.
E-mail address: Ehsani@semnan.ac.ir (M.H. Ehsani).

https://doi.org/10.1016/j.heliyon.2024.e29792
Received 7 September 2023; Received in revised form 29 February 2024; Accepted 15 April 2024
Available online 7 May 2024

from aqueous media with an adsorption rate of 93.6 % in 180 min. In another study, Saad et al. [5] studied the photocatalytic activity of CH/ZnO and CH/Ce–ZnO on the degradation of MG dye (5 mg/L) in the presence of visible light. With 0.02 g and 0.05 g CH/ZnO, the dyes were eliminated after 270 and 90 min, respectively. In addition, using 0.02 g and 0.03 g of CH/Ce–ZnO resulted in the complete removal of 5 mg/L of dye after 90 and 60 min, respectively.

Double perovskite oxide is a compound potentially effective in removing organic dyes. These compounds have the general formula of $A_2BB'O_6$, where A is an alkaline earth or rare earth ion and B and B′ are different transition metal ions. The ideal structure of A_2FeMoO_6 can be visualized as a regular array of corner-sharing FeO_6 and MoO_6 octahedra alternating along the cube axes in all three directions. The A cations occupy the cavities between the octahedra [6,7]. The advantage of double perovskites is that their structural properties can be altered to obtain a suitable band gap to degrade organic dyes in visible and ultraviolet light [8].

According to the literature, the small band gap and the effective surface area of the holes are two critical factors in photocatalytic activity. Although double perovskites have a suitable band gap for photocatalytic activity [8], the latter can be improved by using surfactants. In particular, Li et al. improved the photocatalytic activity of double perovskite Sr_2FeMoO_6 by using EDTA surfactant [8].

The present study aims is to analyze the photocatalytic properties of pure Ba_2FeMoO_6 (BFMO) ferromagnetic double perovskite oxide and a sample containing CTAB (BFMOC), which has not been reported in literature so far. However, the degradation of organic dyes with semiconductor photocatalysts has been studied for decades.

This research uses CTAB surfactant to create porosity and increase absorption sites. Two further aspects that contribute to the utilization of CTAB are the decrease in particle size and the rise in effective surface area. Cetyltrimethylammonium bromide with one hydrophilic end and one hydrophobic end is used to improve the properties of nanomaterials. Research has shown that CTAB can largely prevent particle agglomeration while synthesizing metal nanoparticles as a protective agent. In this respect, CTAB can largely prevent particle agglomeration as a protective agent during nanoparticle synthesis. In addition, it also increases adsorption capacity due to the interaction between surface molecules of CTAB and pollutants [9].

2. Experimental details

The polycrystalline Ba_2FeMoO_6 (BFMO) and the BFMOC sample were synthesized using the conventional sol-gel method (Pechini). The stoichiometric powder amounts of $(NH_4)_6Mo_7O_{24}.4H_2O$, $Fe(NO_3)_3.9H_2O$, and $Ba(NO_3)_2.4H_2O$ were dissolved in deionized water. BFMOC was prepared by dissolving 0.1 g of cetyltrimethylammonium bromide (CTAB) in 10 mL of deionized water and added to this solution. Afterward, it was mixed with nitric acid and ethylene glycol at 70 °*C* until a red gel formed. The gel was dried at 100 °*C* for 12 h, preheated at 300 °*C* in the air for 3 h, and sintered at 900 °*C*. Finally, the powders were pressed into pellets. They were ground with the handy mortar, followed by annealing at 900 °*C* for 10 h in a flow mixture of 5 % H_2 and 95 % Ar in a tube furnace.

The XRD patterns of the samples were analyzed using Cu K radiation with a diffractometer Advance Bruker D-8 with operating at 30 mA, 35 kV, with step of 0.04, and accumulating time 1 s per point. The obtained results were used to confirm the structure and verify the samples' purity phase. Fourier Transform Infrared (FTIR) spectra were acquired using an 8400s-SHIMAZU apparatus with a resolution of 8 cm^{-1} and a scan time of 9 s. The microscopic morphology of the products was examined with FESEM (ZEISS Sigma 300 HV). X-ray photoelectron spectroscopy (XPS) was measured using a BESTEC (EA10) device with 3 % accuracy by the weight on the surface. The N_2 desorption-adsorption isotherm was measured with an instrument (Belsorp-mini X) with an accuracy of ± 1.7 m^2 g^{-1}. Diffuse reflectance analysis was performed with a UV–Vis spectrophotometer (3600-Shimatsu). The UV–Vis spectrum of the samples was recorded with a UV–Vis spectrophotometer (SpecPhoto-A-Vis-NIR). The wavelength measurement accuracy of both UV–Vis spectrophotometers is up to three decimal places in nanometers. A vibrating sample magnetometer with 1 Oe accuracy (VSM, Meghnatis Daghigh Kavir Company, Iran) and a susceptometer (Lake Shore Susceptometer AC700) were used to assess the magnetic properties.

3. Result and discussion

The XRD patterns indicate that the samples have a cubic structure with space group Fm¯3m and single-phase with no discernible impurities. The lattice parameters are a = b = c = 8.069 ± 0.0001 and 8.068 ± 0.0001 Å, and the unit cells are 525.372 and 525.339 $Å^3$ for BFMO and BFMOC, respectively. The average crystallite size and lattice strain of the samples were calculated by the Scherer equation (i.e., $D = \frac{k\lambda}{\beta \cos \theta}$ and $\varepsilon = \frac{\beta}{\tan \theta}$). In this equation, D_{sh}, θ, λ, and β are the crystallite size, the Bragg diffraction angle, the wavelength of the incident X-ray beam (1.5406 Å), and the full width at half maximum (FWHM), respectively. Also, k = 0.9 is a dimensionless shape factor, and ε is lattice strain. Table 1 presents the results of refined structural parameters, the reliability factors, crystallite sizes, and lattice strains of the samples. The Rietveld refinement of the samples shows that the lattice parameters, unit cell volume, and bond lengths decrease compared to the original sample from ($d_{Fe\text{-}O} = 2.0382$ Å, $d_{Mo\text{-}O} = 1.9963$ Å, and $d_{Ba\text{-}O} = 2,8886$ Å)

Table 1
Rietveld refinement structural parameters.

Sample	a = b = c (Å)	V ($Å^3$)	D_{sh} (nm)	ε (%)	R_F	R_p	R_{wp}	R_{exp}	GOF
BFMO	8.069	525.372	95.7	0.103	16.88	65.0	52.4	60.61	0.74
BFMOC	8.068	525.339	95.7	0.103	18.25	53.9	50.1	45.15	1.23

to ($d_{Fe-O} = 2.0381$ Å, $d_{Mo-O} = 1.9962$ Å, and $d_{Ba-O} = 2.8530$ Å). Reducing these parameters with adding CTAB can have an effective role in the magnetic properties of this compound, as will be explained in magnetic properties section. Fig. 1 presents the Rietveld refinement of samples BFMO and BFMOC. XRD patterns of the samples are in good agreement with that reported in the pdf card JCPDS-96-153-3034.

Infrared spectroscopy was used to study the vibrational modes of the synthesized materials. Fig. 2 shows two peaks around 430 cm^{-1} and 829 cm^{-1} for BFMO and BFMOC. The symmetric bending vibrations of Mo–O in the MoO_6 octahedral are responsible for the peaks at 424-430 cm^{-1} [10,11]. In addition, the symmetric stretching vibrations of Mo–O are responsible for the peaks around 815-869 cm^{-1} [8,12]. As can be seen, adding CTAB does not cause a significant change in the absorption peak position along the wavelength. This output demonstrates that the molecular bonding of the sample is unaffected by the addition of CTAB.

FESEM images were used to examine the morphology of the samples. Fig. 3 shows the FE-SEM images, EDX patterns, and maps of the BFMO and BFMOC. As can be seen, the sample's morphology has changed with the addition of CTAB, and many holes have been created. The peaks in the EDX spectra indicate the presence of the elements Ba, Fe, Mo, and O with no impurities. The results confirm the appropriate atomic weight ratio (Table 2). The average grain size for BFMO and BFMOC was calculated using the Digimizer software and the log-normal distribution. For BFMO and BFMOC, the average grain size was about 227 nm and 157 nm, respectively.

In addition, XPS of the BFMO sample was performed to investigate the valence state of elements and surface states. The overall XPS spectra in Fig. 4(a), that the Ba_2FeMoO_6 sample contains Ba 3d, Fe 2p, Mo 3d, O 1s, and C 1s. The peak at 285 eV is associated to C1s line originated by hydrocarbons adsorbed on the surface sample due to its contact with laboratory air and can be used as a calibration peak for the XPS analysis.

Fig. 4(b) presents the XPS spectrum of O 1s, which can be divided into three component peaks. The binding energy peaks at around 530.4 eV, 532.3 eV, and 533.4 eV are assigned to the lattice oxygen in the perovskite structure, surface hydroxyl species, and absorbed water species, respectively. Lattice oxygen, surface hydroxyl, and absorbed content were approximately 62.8 %, 3.50 %, and 33.7 %, respectively. The XPS Fe 2p spectrum consist of two peaks, shown in Fig. 4(c), with the binding energies of 711.93 eV and 723.40 eV attributed to Fe^{3+}. In the Mo spectrum (Fig. 4(d)), two peaks are also observed at 232.44 and 235.85eV, which are indexed to Mo^{5+}. Comparison with literature data on XPS measurements of double molybdates indicate that such binding energies of Mo 3d core-level electrons fit better to the charge state Mo^{6+} [8,13–16]. The XPS spectrums show no mixed valence for the elements at B and B′ sites.

Fig. 5(a) shows the N_2 adsorption–desorption isotherm measurement of BFMO and BFMOC samples. Both catalysts exhibit a typical Type-IV isotherm, and the hysteresis loops are H_4 and H_3 for BFMO and BFMOC, respectively. This result suggests that the absorbents are mesoporous materials (with 2–50 nm) [2]. As shown in Fig. 5(b), the pore size of the BFMO absorbent is between 1-11 nm, while it is 1–9 nm for the sample BFMOC. Table 3 presents the absorbents' specific surface area, pore size, and pore volume. With the addition of CTAB, the specific surface area increases approximately tenfold, and the pore volume is almost twentyfold compared to the parent sample. This result shows an increase in adsorption sites, which can accelerate absorption and shorten the degradation time. Overall, the pore size did not change considerably.

The value of the band gap significantly influences the choice of the type of light source. Accordingly, the band gap energy of BFMO was calculated based on the Kubelka-Munk (2, 3) and Tauc's (1) formulas, as follow [17–22]:

$$h\nu = \frac{hc}{\lambda} = \frac{1239.8}{\lambda}\ \text{eV} \tag{1}$$

$$(F(R).h\nu)^n = B\left(h\nu - E_g\right) \tag{2}$$

$$F(R) = (1-R)^2/2R \tag{3}$$

where n is 2 for the direct and 1/2 for the indirect band gap.

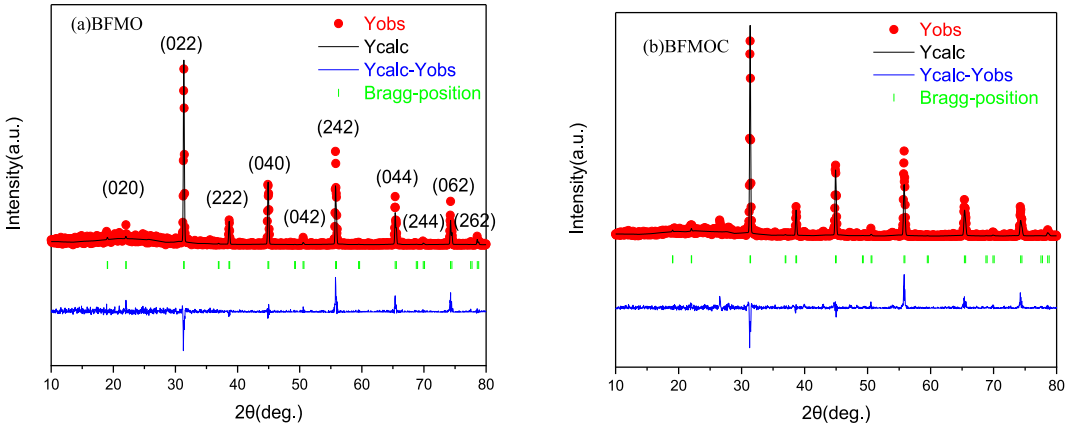

Fig. 1. Rietveld refinement of XRD pattern for (a) BFMO and (b) BFMOC.

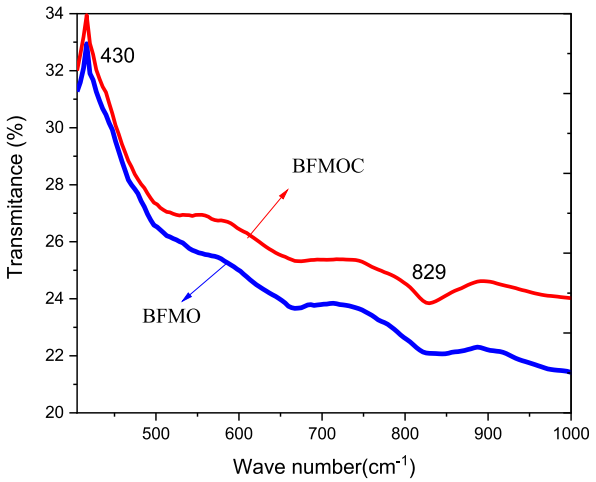

Fig. 2. FTIR spectra of BFMO and BFMOC.

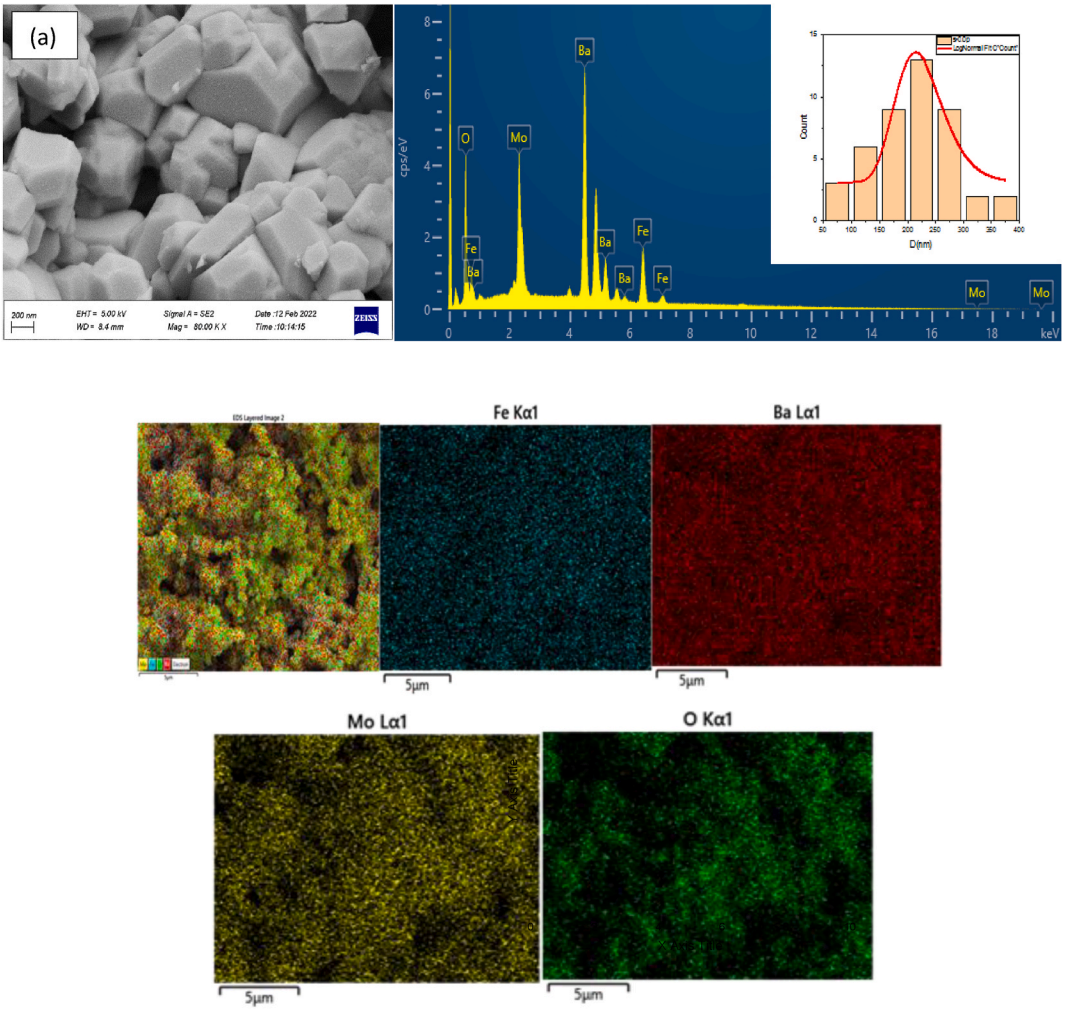

Fig. 3. FESEM image and EDX pattern of (a) BFMO and (b) BFMOC.

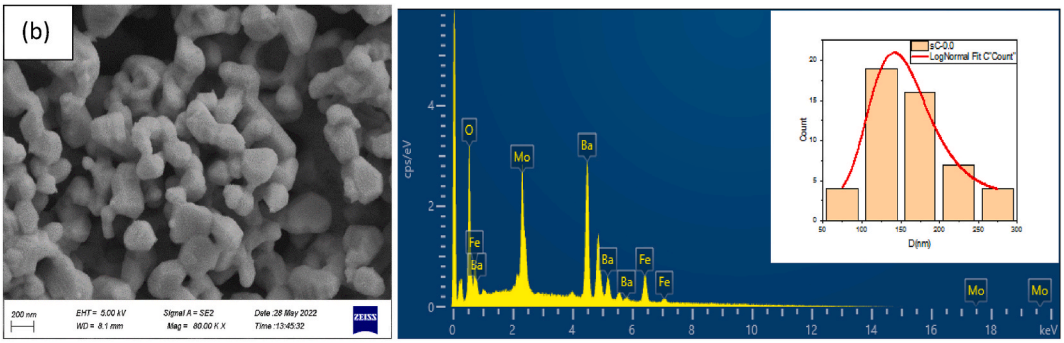

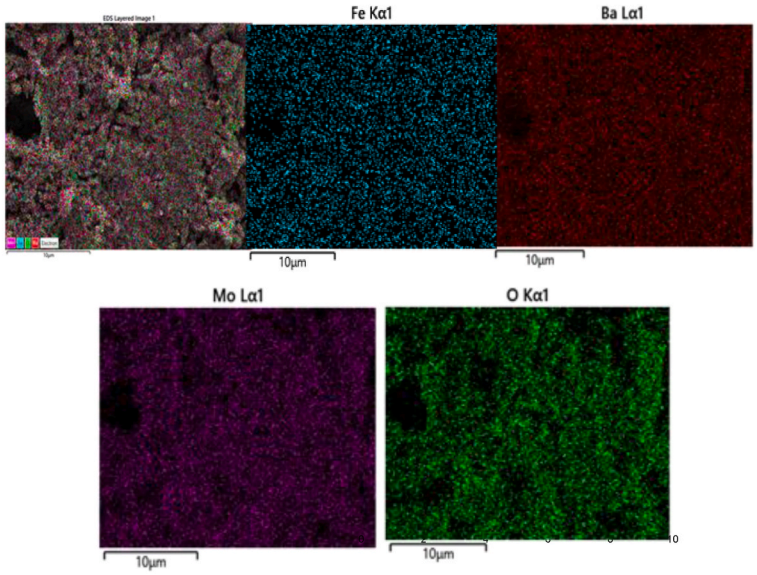

Fig. 3. (*continued*).

Table 2
Atomic weight ratio of the samples.

Map Sum Spectrum	BFMO	BFMOC
Element	**Atomic %**	**Atomic %**
O	67.33	65.77
Fe	7.64	7.65
Ba	16.88	17.55
Mo	8.15	9.03
Total	100.00	100.00

Fig. 6(a) shows two distinct absorption peaks for DRS spectra of parent sample. These two absorption cut-offs correspond to two possible band gaps. The two absorption bands are ascribed to the charge transfer from oxygen (2p) electrons that moved into the central molybdenum atom inside the MoO_6 and FeO_6 octahedra [8,23,24]. Moreover, the absorption peak at the higher wavelength in the parent sample may be associated with the Fe^{3+} d-d level transition or the charge transfer transition between the ions [8].

Fig. 6(b) presents the band gap energy of the parent sample (~2.43 eV) versus photon energy. According to similar reports related to double perovskite samples [8], the band gap determined for the parent sample can be attributable to the direct band gap.

The UV–Vis spectrum of the BFMOC sample (Fig. 7(a)) shows two absorption peaks at 223 nm and 705 nm in the ultraviolet and visible regions, respectively. Fig. 7(b) shows the direct (~2.29 eV) and band gap energy of the BFMOC versus the photon energy. These band gaps may lead to the photocatalytic activity of the samples in the visible light range [8]. According to the absorption peak corresponding to the CTAB-containing sample at 705 nm (E = 1.75eV), this compound can absorb visible light at this wavelength. For this sample, the band gap energy of 1.71 eV can be related to the wavelength of 705 nm, which can be considered the direct band gap.

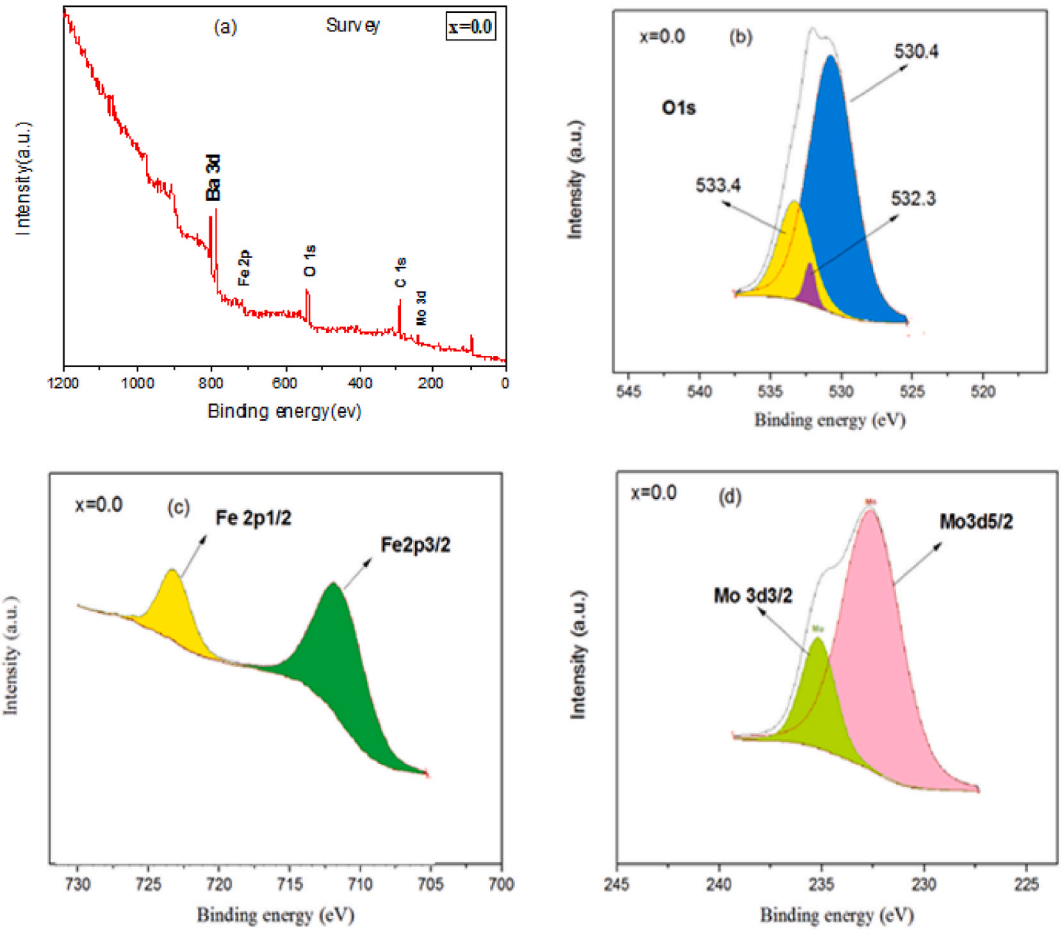

Fig. 4. XPS patterns of BFMO (a) survey, (b) O 1s, (c) Fe 2p, and (d) Mo 3d

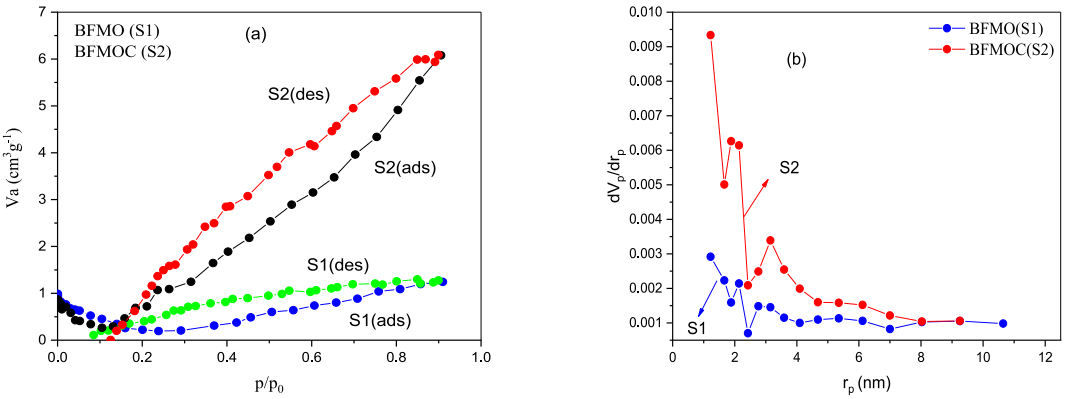

Fig. 5. BET analysis of (a) Nitrogen adsorption–desorption isotherms and (b) pore size distribution of BFMO and BFMOC.

The performance of a photocatalyst is determined by two main factors: narrow band gap and specific surface area of the catalyst. The high specific surface area can highly adsorb dye on its surface, and the small band gap can enhance visible light absorption [8]. When light radiates on an absorbent, electrons in the valence band are excited and moved up to the conduction band, thereby, forming some holes in the valence band. Fig. 8 illustrates a schematic diagram of the charge carrier transfer process and the photocatalytic mechanism of the sample. The photoelectrons generated on the conduction band react with the O^{2-} on the surface and reduce the O^{2-} to.O^{2-} superoxide radicals. Free radicals are generated when electrons and holes are present in an aqueous solution. Photo-generated holes can react directly with H_2O and OH^- to produce •OH radicals, which are strong oxidants. Pollution is eliminated when free

Table 3
BET analysis results.

Sample	Specific surface area (m^2/g)	Total pore volume (cm^3/g)	Average pore size (nm)
BFMO	0.95	3.78×10^{-4}	1.88
BFMOC	10.36	78.56×10^{-4}	1.66

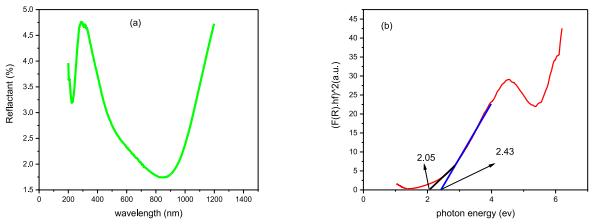

Fig. 6. (a) DRS spectra and (b) the direct band gap energy of BFMO.

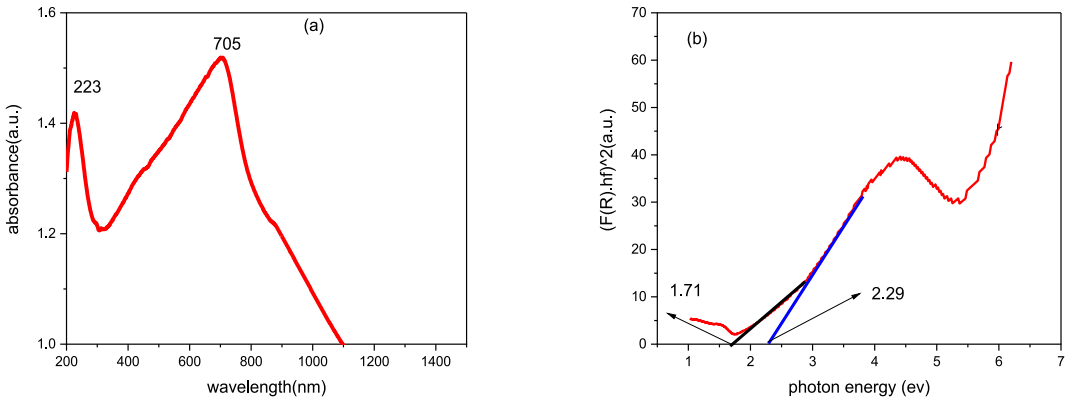

Fig. 7. (a) UV–Vis and (b) the direct band gap energy of BFMOC.

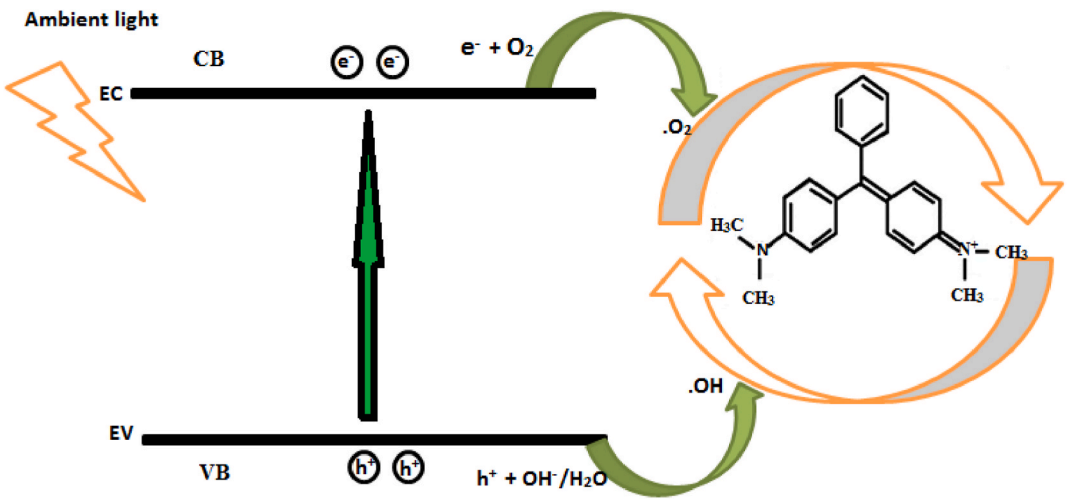

Fig. 8. Schematic diagram of charge carrier transfer process and photocatalytic mechanism of the sample.

radicals interact with water pollutants. O^{2-} and •OH are active species that can directly attack the MG molecule and decolorize the dye [8,13].

The malachite green dye under visible light irradiation was degraded using natural light without a light source such as a lamp. The natural pH of the solutions was ~5. While stirring the dye solution with a mechanical stirrer, 2.5 ml of the solution was removed and centrifuged at 4000 rpm for 2 min every 5 min. Meanwhile, the absorption spectra of the samples were recorded immediately with a UV–Vis spectrophotometer.

To sudy the effect of the amount of catalyst on the degradation time of malachite green (MG), 0.005 and 0.03 g of absorbent (BFMO) were poured into 100 mL of 10 ppm MG aqueous solution and placed under ambient light. Fig. 9 shows the degradation of 10 ppm MG dye in (a) 70 min and (b) 6 min using 0.005 g and 0.03 g of the catalyst in 100 mL of solution, respectively.

Fig. 10 shows the degradation of 100 ml of 40 ppm MG dye under ambient light for (a) 160 min and (b) 20 min using 0.01 g and 0.03 g of the sorbent, respectively. In both figures, the sudden drop in the absorption peak with the addition of the catalyst may indicate that the BFMO sample has absorption properties. The MG dye degradation can be explained by the decrease in the absorption peaks over time. Figs. 9 and 10 indicate that the amount of catalyst significantly affects the degradation rate, indicating that the absorption sites increase with increasing the absorbent content. Therefore, the adsorption capacity of the dye is increased [2]. In this respect, a comparable trend was reported by Muinde et al. [4] and Saad et al. [5].

This effect was examined for four concentrations of MG (10 ppm, 40 ppm, 60 ppm, and 100 ppm). About 0.03 g of absorbent was poured into 100 ml of MG and tested as mentioned above. As can be seen from Fig. 11, the degradation time increased from 6 min to 40 min by increasing the dye concentration. This increase may be due to the limited number of sites available in a given amount of absorbent. A clear reduction in peaks was observed at lower concentrations of MG. Dye concentration directly affects the dye removal process [4]. The present study showed that as the initial concentration increased, the absorption decreased. The explanation is that the catalyst's surface was covered with dye molecules, and weak absorbent-adsorbate interactions appeared [4,5].

The initial dye removal rate increases rapidly, which may be due to the presence of a large number of adsorption sites. As the adsorption reaction proceeds, the dye molecules on the adsorbent surface diffuse gradually inward until reaching equilibrium when the dye covers all active sites [2].

The kinetics of degradation were also studied using the results obtained by varying the concentration as a function of time. The catalytic decomposition kinetics of organic dyes generally follows the Langmuir-Hinshelwood mechanism [1,25,26]:

$$r = -dc/dt = K_{app}\, C \tag{4}$$

where r is the reagent degradation rate ($mg.L^{-1}\ min^{-1}$), t is the reaction rate during irradiation, C is the reagent concentration ($mg.L^{-1}$), and K_{app} is the constant number of the apparent reaction rate (L/mg).

When C is too small, it can be simplified to Eq. (5):

$$-Ln(C / C_0) = K_{appa}\, t \tag{5}$$

K_{appa} is the apparent first-order rate constant given by the slope of the plot of $ln(C/C_o)$ versus t, while $ln(C/C_0)$ reperesents the natural logarithm of the initial concentration to the concentration at time t of the reagent.

For the sample BFMO, the plots of $ln(C/C_o)$ versus time show that K_{appa} is 0.24, 0.17, 0.08, and 0.05 min^{-1} for different concentrations of MG (i.e., 10 ppm, 40 ppm, 60 ppm, and 100 ppm, respectively). After adding the absorbent, the dye was first absorbed and then dispersed in room light (Fig. 12(a–d)).

The percentage of dye removal is calculated by Eq. (6) [2,27–29]:

$$\%\ \text{Removal} = [(C_0 - C) / C_0] \times 100\% \tag{6}$$

Fig. 12(e) represents the dye removal at different MG concentrations. Removal rates are 100 %, 100 %, 97.5 %, and 91.2 % at 6, 20, 30, and 40 min, respectively. Lower concentrations of MG increase the absorption sites and thus accelerating the elimination rate [4].

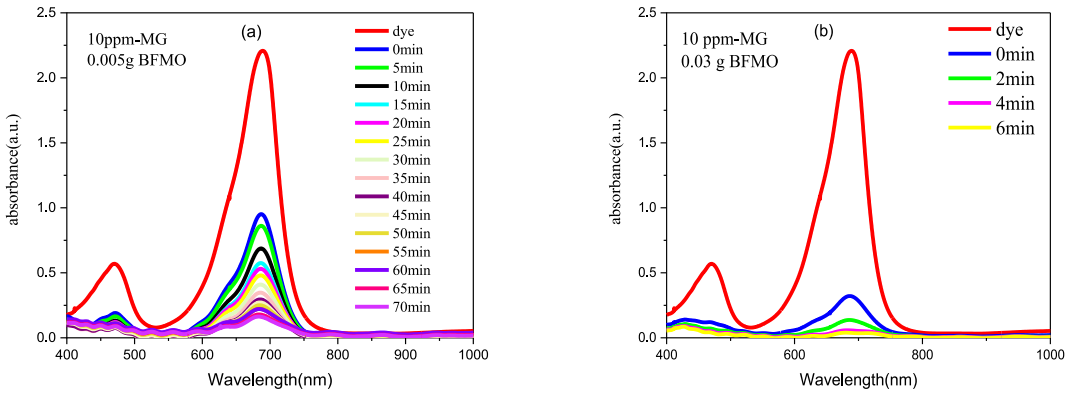

Fig. 9. Visible absorption spectra of (a) 0.005 g and (b) 0.03 g BFMO in 100 ml MG 10 ppm.

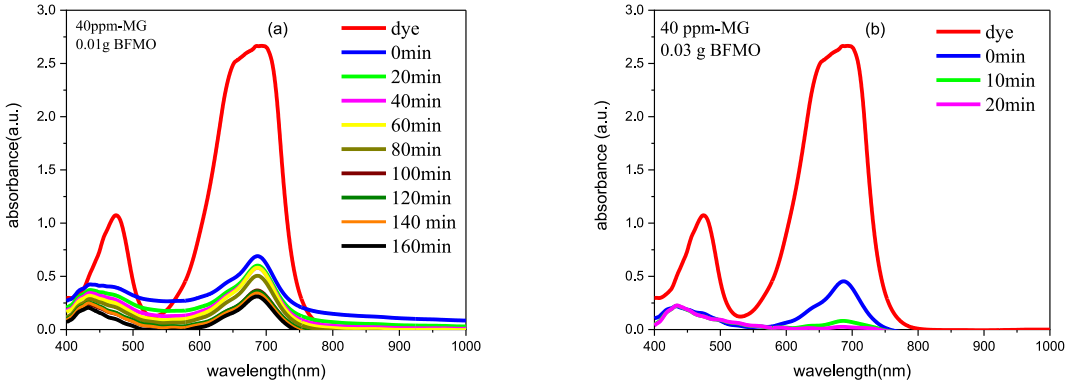

Fig. 10. visible absorption spectra of (a) 0.01g and (b) 0.03g BFMO in 100 ml MG 40 ppm.

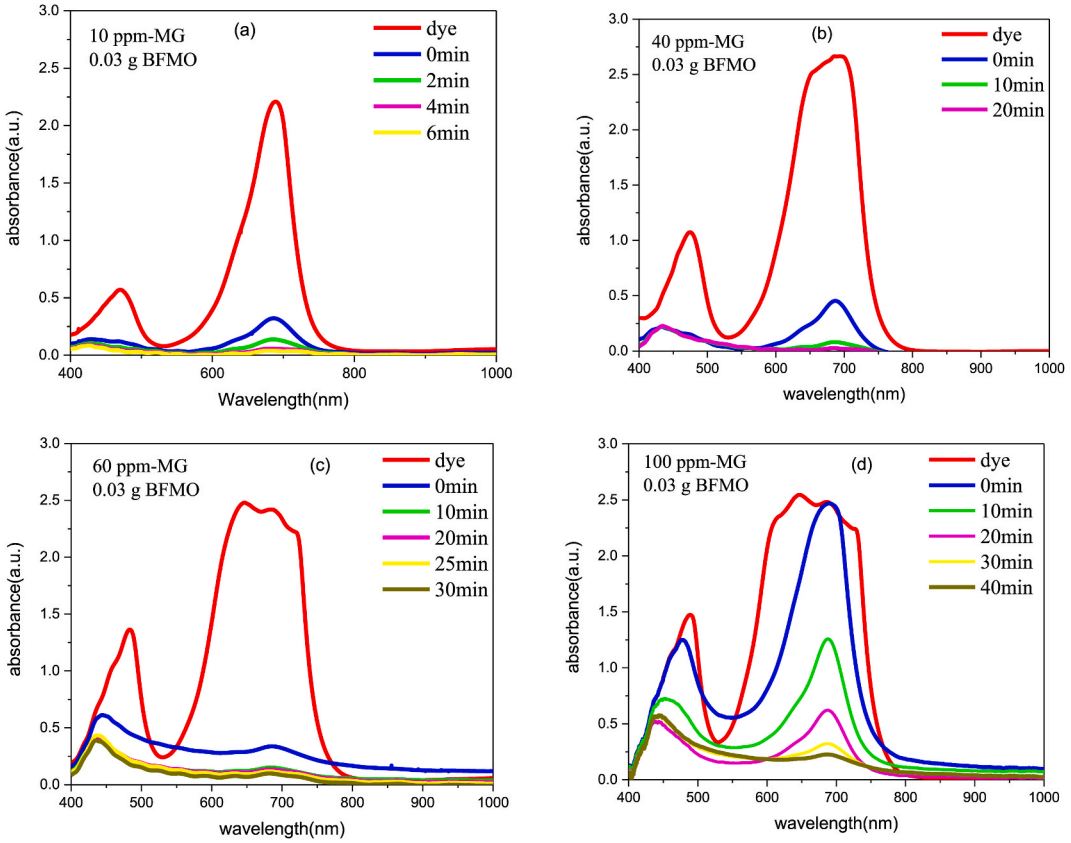

Fig. 11. Vis. spectra 0f 0.03 g BFMO in100 ml MG solution (a) 10 ppm, (b) 40 ppm, (c) 60 ppm,and (d) 100 ppm.

The adsorption-desorption effect was investigated by adding 0.03 g of BFMO and BFMOC catalysts to 100 ml of 100 ppm MG and leaving it for 1 h in the dark. The samples were then exposed to ambient light. Absorption spectra of the samples were recorded every 20 min in the dark and every 5 min in the light. Fig. 13(a) shows that the absorption spectrum is significantly reduced compared with the sample shown in Fig. 11(d), which was examined under ambient light. Fig. 13(b) shows that the absorption peak is significantly reduced in the dark, probably due to the presence of pores and large specific surface area in the BFMOC sample (Table 3). This result indicates the role of CTAB. Furthermore, active oxide radicals are generated by reducing the band gap energy, which is favorable for the excitation of external electrons (Fig. 7) [5].

In addition, 0.005 g of BFMO and BFMOC catalysts in 100 ml of 10 ppm MG were examined. In a dark place, the absorption spectrum of the BFMO sample decreased for 1 h. After exposure to ambient light, the absorption intensity increased significantly during the first 5 min (Fig. 14(a)). This data is, consistent with the absorption intensity after 20 min in the dark, probably due to the

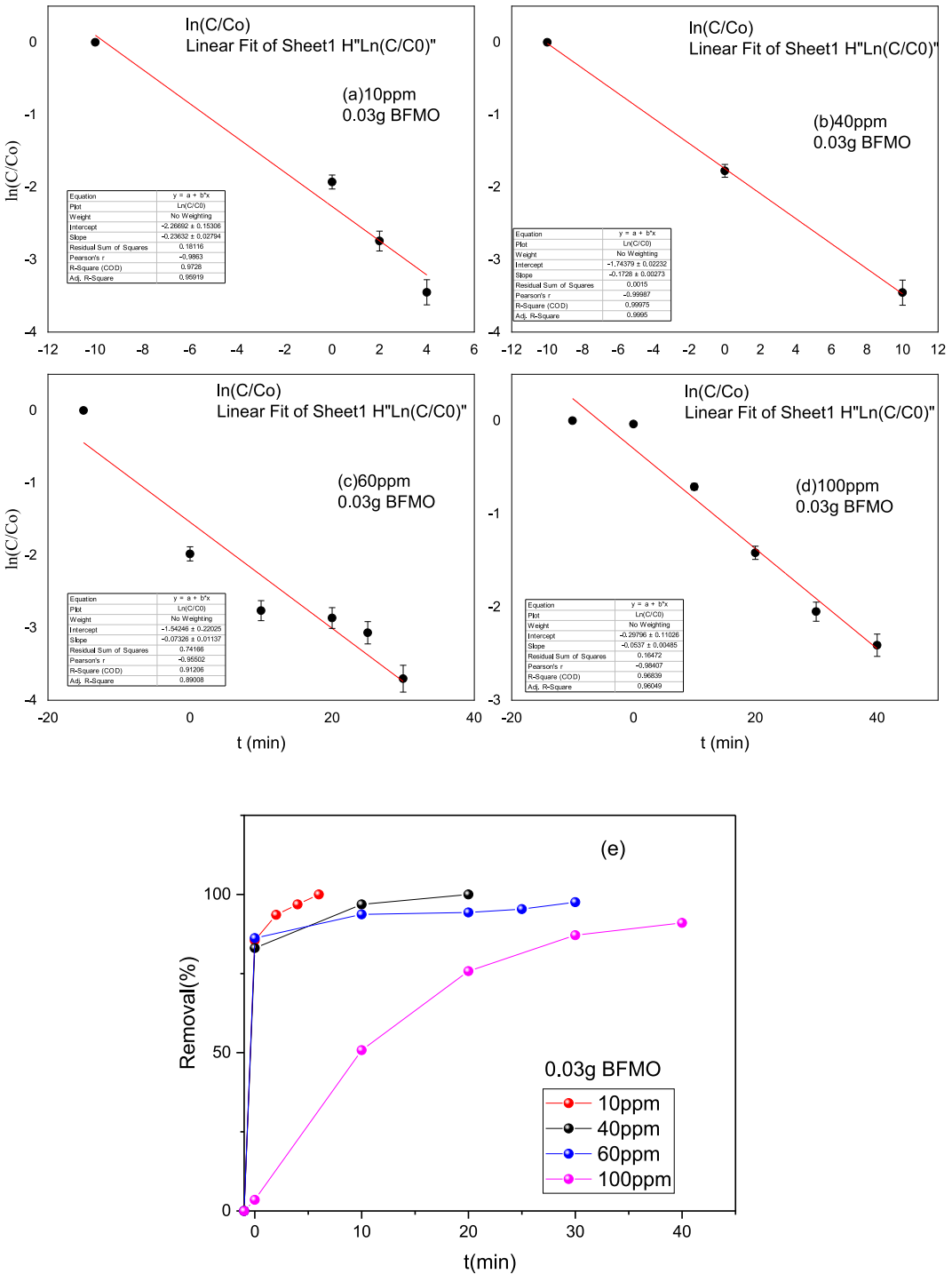

Fig. 12. (a–d) ln(C/C$_o$) and (e) the percentage of removal of 0.03 g BFMO Vs. time, in 10 ppm,40 ppm,60 ppm, and100 ppm MG aqueous solutions.

recombination of electrons and holes in the solution [5]. After 50 min in room light, the dye solution was removed by about 100 %. The addition of CTAB caused dye removal in the BFMOC sample (Fig. 14(b)), which was explained by the increase in specific surface area and the presence of pores [2].

Fig. 15 illustrates the absorption spectra of the sample BFMOC tested in a dark place. The 100 % degradation rates from 10 ppm MG occurred in 5 min. This effect is related to the fact that the adsorbent has a specific surface area and many available sites (e.g., pores) that adsorb the dye molecules. The noteworthy point in this figure is the adsorption effect instead of a photocatalytic process.

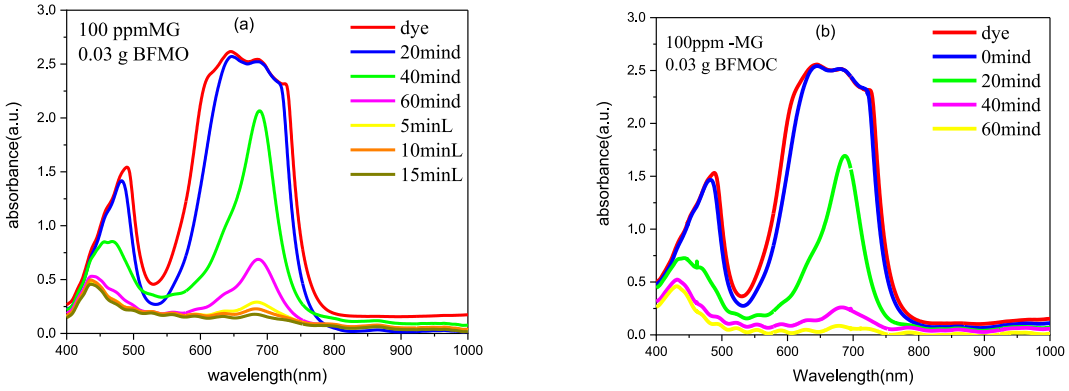

Fig. 13. Visible absorption spectra of 0.03 g catalyst (a) BFMO and (b) BFMOC in 100 ml MG 100 ppm, with adsorption-desorption step.

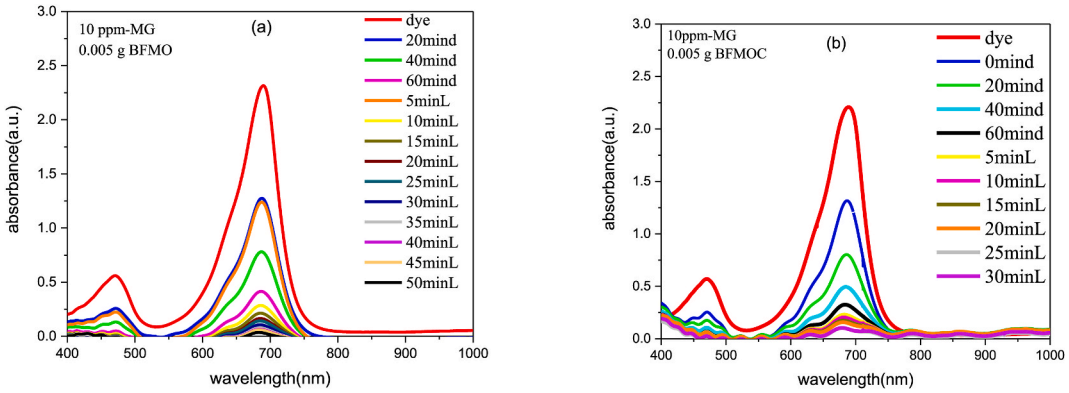

Fig. 14. Visible absorption spectra of 0.005 g catalyst (a)) BFMO and (b) BFMOC in 100 ml MG 10 ppm, with adsorption-desorption step.

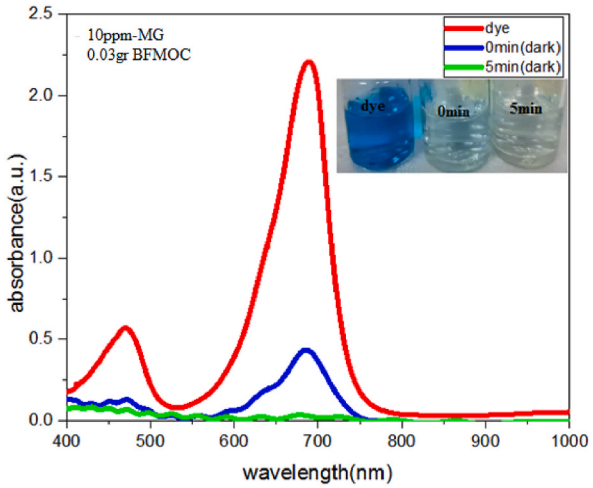

Fig. 15. Absorption spectra of 0.03 g BFMOC in 10 ppm MG with adsorption-desorption step.

The intensity effect of the light was checked by performing the above test again for the BFMOC sample on a cloudy day (Fig. 16). According to Fig. 16(a), the absorption peak changes very slowly, but its intensity does not change in the dark. When placed in the ambient light, the absorption peak reduction occurred slower than in Fig. 13(a) and (b).

For further investigation, 100 ml of 10 ppm MG was mixed with 0.005 g of BFMOC catalyst to repeat the above test. In the dark, the addition of BFMOC results in a reduction in the absorbance peak (Fig. 16(b)). However, when the sample is placed in the room light,

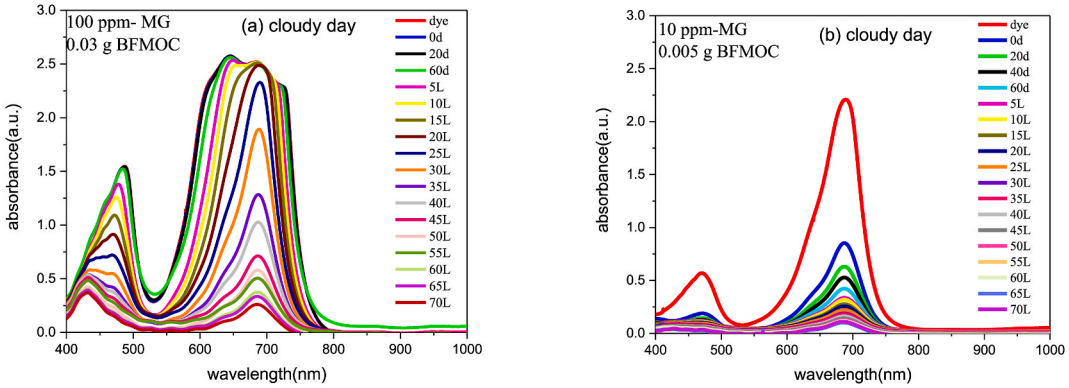

Fig. 16. Visible absorption spectra of (a) 0.03 g BFMOC in 100 ml MG100 ppm and (b) 0.005 g BFMOC in 100 ml MG 10 ppm, with adsorption-desorption step, on a cloudy day.

the peak reduction is less than when adding BFMO at the same time (Fig. 14a and b). Under these circumstances, BFMOC also experiences a longer degradation time. This difference can be attributed to the room's decreased in light intensity because the excited electrons are not energetic enough to cause oxidation of the dye molecules [30]. With reduced ambient light, fewer electrons are excited, thereby reducing the generation of active hydroxyl radicals and the photocatalytic oxidation rate.

Table 4 compares results obtained from the current study and the other MG dye removal studies. The table shows the use of different absorbents to degrade malachite green solution with different concentrations and different removal rates. For instance, 0.03 g of CH/Ce–ZnO degraded 100 ml of 5 ppm MG in 60 min [5], 1.5 g $MnFe_2O_4$ degraded 100 ml of 50 ppm MG at the same time by adding H_2O_2 [1], or 100 ml 15 ppm MG dye was removed using 0.2 g ZnO/CuO under a UV source while adjusting the solution pH to 10 [28].

According to Table 4, BFMO in this work shows 100 % dye removal of 100 ml MG 40 ppm in 20 min using 0.03 g absorbent without adding H2O2 or changing the pH.

For BFMOC, dye removal from 100 ml of 10 ppm malachite green solution occurred in 5 min in a dark place, which was not previously reported. Also, this compound degrades the malachite green on a cloudy day without using a lamp as a source.

4. Magnetic properties

The magnetic properties of these materials were examined as a function of temperature. To this end, the susceptibility of the samples was measured with an AC susceptometer at a frequency of 333 Hz and temperatures of 70–330K in a fixed magnetic field (800 A/m^2).

The temperature dependency of the real and imaginary parts of the AC susceptibility of the samples is shown in Fig. 17. As can be seen in Fig. 17(a) and (b), the real and imaginary parts of the susceptibility of BFMOC decrease with respect to BFMO. The presence of a peak in the imaginary part of the magnetic susceptibility is attributed to the transition temperature (T_c). Compared with the transition temperature of the BFMO sample, the critical temperature of the BFMOC exhibits an increase in this value. Here, T_c can be influenced

Table 4
Comparison of the efficiency of removing the MG obtained by other works and this work.

sample	Initial Concentration (mg/L)	Adsorbent (g)	Removal (%)	Time (min)	pH	Reference
$MnFe_2O_4 + H_2O_2$	50	1.5	~100	60		[1]
CS–ZnO	9.3	1.2	80.1	180		[4]
CH/ZnO	5	0.02	100	270		[5]
CH/ZnO	5	0.05	100	90		[5]
CH/Ce–ZnO	5	0.02	100	90		[5]
CH/Ce–ZnO	5	0.03	100	60		[5]
ZnO/CuO (UV)	15	0.2	99	120	10	[28]
BFMO	10	0.005	99.87	50		current work
BFMO	10	0.03	100	6		current work
BFMO	40	0.01	88.05	160		current work
BFMO	40	0.03	100	20		current work
BFMO	60	0.03	97.5	30		current work
BFMO	100	0.03	91.02	40		current work
BFMOC(dark)	10	0.03	100	5		current work
BFMOC(dark)	100	0.03	100	60		current work
BFMOC(Cloudy)	10	0.005	97	70		current work
BFMOC(Cloudy)	100	0.03	90	70		current work
BFMOC	10	0.005	95.17	30		current work

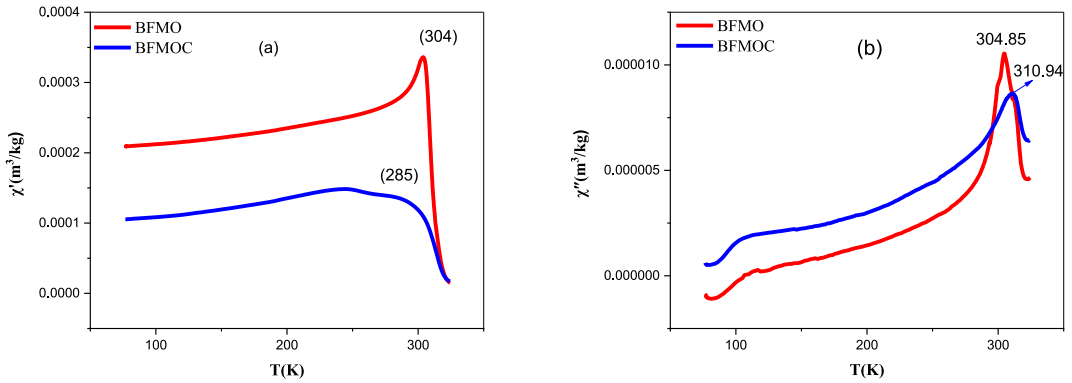

Fig. 17. BFMO and BFMOC Ac susceptibility, (a) real part and (b) imaginary part.

by steric, electron injection, and anti-site defects [31].

The reduction in lattice parameters can also have an effective role in the magnetic properties of double perovskites compounds because it can affect the exchange interactions between the magnetic ions. In Ba_2FeMoO_6, the Fe and Mo ions are antiferromagnetically coupled, meaning they have opposite spin directions. The strength of this coupling depends on the distance between the Fe and Mo ions, which is related to the lattice parameters. By reducing the lattice parameters, the distance between the Fe and Mo ions decreases, which can increase the strength of the antiferromagnetic coupling. This can lead to an increase in the magnetic ordering temperature [32].

The magnetic properties of the samples were examined with a VSM instrument. The results demonstrate the ferromagnetic behavior of both samples. As shown in Fig. 18, the saturation magnetization (M_s) and remanent magnetization (M_r) of the BFMO sample decrease from ~1.43 to ~0.89 μ_B/f.u and from ~0.075 to ~0.054 μ_B/f.u with addition CTAB, respectively. The decrease in M_s may be attributed to an increase in the holes in the materials by decreasing magnetic material in determined volume and blocking transfer electrons between grains due to the holes. The coercive field of the BFMOC sample also increases from ~21 Oe to ~32 Oe at room temperature, which is attributed to the decrease in magnetic properties. The increase in the coercive field is likely due to the presence of pores and the separation of magnetic particles due to the addition of CTAB. As a result, magnetic interaction between nanoparticles decline [33]. Another factor that reduces magnetization could be a decrease in particle size [34].

5. Conclusion

Finally, two samples were synthesized to compare their photocatalytic properties. The addition of CTAB led to no significant change in the lattice parameters and crystallite size of the sample. Adding CTAB did not cause a significant change in the absorption peak position along the wavelength in FTIR analyses. This result can state that the molecular bonding of the sample is unaffected by the addition of CTAB. However, the sample's morphology changed and more pores were generated, resulting in more dye absorption. The XPS spectrums of the parent sample showed no mixed valence for the elements at B and B′ sites. The results of BET analyses suggested that both absorbents were mesoporous materials. DRS spectra of the samples showed direct band gaps (~2eV) for both samples. The photocatalytic activities show that complete removal was achieved after 6 min and 20 min by adding 0.03 g of pure Ba_2FeMoO_6 to 10

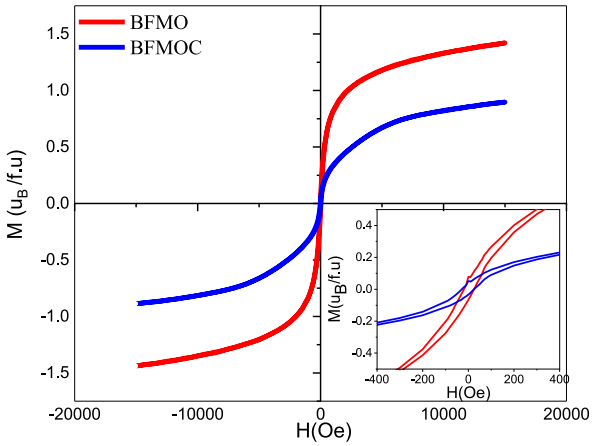

Fig. 18. Curve of magnetization of BFMO and BFMOC, at room temperature (Inset: hysteresis loops).

ppm and 40 ppm MG dye, respectively. Moreover, the degradation percentage can reach about 98 % for 60 ppm after 30 min and 92 % for 100 ppm dye concentration after resting 40 min in the light room. For 0.03 g of BFMOC, which is contented with CTAB, 100 ml of 10 ppm MG degraded 100 % in 5 min in the dark. In cloudy weather, the dye removal time was prolonged. The removal rate of pollutants from aqueous solutions is controlled to a large extent by the absorbent dosage and dye concentration. The results showed that BFMO is an excellent adsorbent without adding H_2O_2 and with very high adsorption to degrade the toxic aqueous solution of MG at natural pH and ambient light. Nevertheless, BFMOC is ten times more effective regarding its special surface area and total pore volume. Compare to literature BFMO and BFMOC are more effective in degradation of MG dye. The sample BFMOC's critical temperature increased compared to BFMO, and saturation magnetism decreased. This sample shows a higher coercive field than the BFMO sample due to less interaction between the magnetic nanoparticles and the presence of more holes.

Availability

The datasets used and/or analyzed during the current study are available upon reasonable request from the corresponding author. The data associated with our study has not been deposited into a publicly available repository.

CRediT authorship contribution statement

Z. Ghorbani: Writing – review & editing, Writing – original draft, Visualization, Validation, Supervision, Software, Resources, Project administration, Methodology, Investigation, Funding acquisition, Formal analysis, Data curation, Conceptualization. **M.H. Ehsani:** Writing – review & editing.

Declaration of competing interest

The authors declare that they have no known competing financial interests or personal relationships that could have appeared to influence the work reported in this paper.

References

[1] F.V. de Andrade, A.B. de Oliveira, G.O. Siqueira, M.M. Lage, M.R. de Freitas, G.M. de Lima, J. Nuncira, $MnFe_2O_4$ nanoparticulate obtained by microwave-assisted combustion: an efficient magnetic catalyst for degradation of malachite green cationic dye in aqueous medium, J. Environ. Chem. Eng. 9 (2021) 106232.

[2] X. Fan, L. Deng, K. Li, H. Lu, R. Wang, W. Li, " Adsorption of malachite green in aqueous solution using sugarcane bagasse-barium carbonate composite", Colloid and Interface Science Communications 44 (2021) 100485.

[3] J. Yousheng, C. Li, H. Kun, Y. Wenjuan, Y. Xianle, L. Liqun, "Development of a Fast ELISA for the specific detection of both Leucomalachite green and malachite green", J. Ocean Univ. China 14 (2015) 340–344. ISSN.

[4] V.M. Muinde, J.M. Onyari, B. Wamalwa, J.N. Wabomba, "Adsorption of malachite green dye from aqueous solutions using mesoporous chitosan–zinc oxide composite material", Environmental Chemistry and Ecotoxicology 2 (2020) 115–125.

[5] A.M. Saad, M.R. Abukhadra, S.A. Ahmed, A.M. Elzanaty, A.H. Mady, M.A. Betiha, J.J. Shim, A.M. Rabie, Photocatalytic degradation of malachite green dye using chitosan supported ZnO and Ce–ZnO nano-flowers under visible light, J. Environ. Manag. 258 (2020) 110043.

[6] Imad Hussain, M.S. Anwar, S.N. Khan, Aga Shahee, Zeeshan Ur Rehman, Bon Heun Koo, Magnetocaloric effect and magnetic properties of the isovalent Sr^{2+} substituted Ba_2FeMoO_6 double perovskite, Ceram. Int. 43 (2017) 10080–10088.

[7] S. Tajima, S. Miyasaka, S.A. Saafan, T.M. Meaz, M.K. El Nimr, R.E. El- Shater, Curie temperature enhancement with reserving a reasonable magnetoresistance by Pr substitution in Ba_2FeMoO_6, J. Magn. Magn Mater. 435 (2016) 1–8.

[8] X.Y. Li, Z.F. Yao, L.Y. Zhang, G.H. Zheng, Z.X. Dai, K.Y. Chen, Generation of oxygen vacancies on Sr_2FeMoO_6 to improve its photocatalytic performance through a novel preparation method involving pH adjustment and use of surfactant, Appl. Surf. Sci. 480 (2019) 262–275.

[9] L. Gan, Z. Lu, D. Cao, Z. Chen, Effects of cetyltrimethylammonium bromide on the morphology of green synthesized Fe_3O_4 nanoparticles used to remove phosphate, Mater. Sci. Eng. C 82 (2018) 41–45.

[10] M. Bazarganipour, Synthesis and characterization of $BaMoO_4$ Nanostructures prepared via a Simple Sonochemical Method and their degradation ability of methylene blue, Ceram. Int. 42 (2016) 12617–12622.

[11] S. Feraru, P. Samoila, A.I. Borhan, M. Ignat, A.R. Iordan, M.N. Palamaru, Synthesis, characterization of double perovskites Ca_2MSbO_6 (M = Dy, Fe, Cr, Al) materials via sol-gel auto-combustion and their catalytic properties, Mater. Char. 84 (2013) 112–119.

[12] Y.A. Alsabah, A.A. Elbadawi, E.M. Mustafa, M.A. Siddig, The effect of Replacement of Zn^{2+} cation with Ni^{2+} cation on the structural properties of $Ba_2Zn_{1-x}Ni_xWO_6$ double perovskite oxides (X = 0, 0.25, 0.50, 0.75, 1), J. Mater. Sci. Chem. Eng. 4 (2016) 61–70.

[13] L. Xu, Y. Wan, H. Xie, Y. Huang, L. Yang, L. Qin, H. Jin Seo, "Synthesis, surface structure and optical properties of double perovskite Sr_2NiMoO_6 nanoparticles", Appl. Surf. Sci. 389 (2016) 849–857.

[14] V.V. Atuchin, O.Y. Khyzhun, O.D. Chimitova, M.S. Molokeev, T.A. Gavrilova, B.G. Bazarov, J.G. Bazarova, Electronic structure of β-$RbNd(MoO_4)_2$ by XPS and XES, J. Phys. Chem. Solid. 77 (2015) 101–108.

[15] S.F. Solodovnikov, V.V. Atuchin, Z.A. Solodovnikova, O.Y. Khyzhun, M.I. Danylenko, D.P. Pishchur, P.E. Plyusnin, A.M. Pugachev, T.A. Gavrilova, A. P. Yelisseyev, A.H. Reshak, Z.A. Alahmed, N.F. Habubi, Synthesis, structural, Thermal, and electronic properties of Palmierite-related double molybdate α-$Cs_2Pb(MoO_4)_2$, Inorg. Chem. 56 (2017) 3276–3286.

[16] Y. Hu, S. Wang, X. Wang, Y. Tang, Effects of vacancy doping at the Mo site on the magnetic property of double perovskite Sr_2FeMoO_6, Physica B 583 (2020) 412023.

[17] M.D.I. Bhuyan, S. Das, M.A. Basith, Sol-gel synthesized double perovskite Gd_2FeCrO_6 nanoparticles: structural, magnetic and optical properties, J. Alloys Compd. 878 (2021) 160389.

[18] M. Hemmati, M. Jafar Tafreshi, M.H. Ehsani, S. Alamdari, Highly sensitive and wide-range flexible sensor based on hybrid $BaWO_4$@CS nanocamposite, Ceram. Int. 48 (2022) 26508–56518, https://doi.org/10.1016/j.ceramint.2022.05.347.

[19] E. Farahi, N. Memarian, Surfactant-assisted synthesis of Ni_2P nanostructures: effect of surfactant concentration on photocatalytic activity, Eur.phys.J.plus 137 (2022) 463.

[20] M. Hosseinpour, H. Abdoos, O. Mirzaee, S. Alamdari, Fabrication and Characterization of a new flexible ionizing ray sensor based on lead tungstate ($PbWO_4$), Ceram. Int. 49 (2022) 4722–4732.

[21] S. Alamdari, M. Sasani Ghamsari, M. Jafar Tafreshi, Optimization of Gallium concentration to improve the performance of ZnO nanopowders for nanophotonic applications, Ceram. Int. 46 (2020) 4484–4492.
[22] S. Esmaeili, M.H. Ehsani, M. Fazli, Photo-catalytic activities of La0.7Ba 0.3MnO3 nanoparticles, Optik - International Journal for Light and Electron Optics 216 (2020) 164812.
[23] Y.N. Zhu, G.H. Zheng, Z.X. Dai, L.Y. Zhang, Y.Q. Ma, Photocatalytic and luminescent properties of $SrMoO_4$ phosphors prepared via hydrothermal method with different stirring speeds, J. Mater. Sci. Technol. 33 (2017) 23–29.
[24] Y. Luo, J.W. Xue, X.D. Zhu, J. Daniel, X. Gao, S. Sun, C. Gao, J. Bao, Enhanced photocatalytic oxygen evolution over Mo-doped Ca_2NiWO_6 perovskite photocatalyst under visible light irradiation, RSC Adv. 7 (2017) 5821–5826.
[25] A. Arabi, M. Fazli, M.H. Ehsani, Tuning the morphology and photocatalytic activity of La0.7Ca0.3MnO3 nanorods via different mineralizer-assisted hydrothermal syntheses, Mater. Res. Bull. 90 (2017) 205–211.
[26] A. Arabi, M. Fazli, M.H. Ehsani, Photocatalytic activity of the La.7Ca0.3MnO3 nanorods, Progress in Physics of Applied Materials 2 (2022) 123–131.
[27] S. Esmaeili, M.H. Ehsani, M. Fazli, Structural, optical and photocatalytic properties of La0.7Ba0.3MnO3 nanoparticles prepared by microwave method, Chem. Phys. 529 (2019) 110576.
[28] L. Anju Chanu, K. Jugeshwar Singh, K. Nomita Devi, " UV light illuminated photodegradation of Malachite green dye using ZnO/CuO nanocomposites", Mater. Today: Proc. 65 (2022) 2865–2870.
[29] K. Adesina Adegoke, I. Adewale Bello, O. Solomon Bello, M. Adeyemi Balogun, N. Wendy Maxakato, Modification of cellulosic material for rapid dyeability with malachite green dye, Scientific African 16 (2022) e01138, https://doi.org/10.1016/j.sciaf.2022.e01138.
[30] M. Tsvetkov, J. Zaharieva, M. Milanova, Ferrites, modified with silver nanoparticles, for photocatalytic degradation of malachite green in aqueous solutions, Catal. Today 357 (2020) 453–459.
[31] J. Kim, J.G. Sung, H.M. Yang, B.W. Lee, Effects of carrier doping on Curie temperature in double perovskite Ba_2FeMoO_6, J. Magn. Magn Mater. 290–291 (2005) 1009–1011.
[32] Q. Zhang, G.Y. Liu, Z.F. Xu, X.M. Feng, G.H. Rao, Structural and magnetic properties of rare-earth doped $(Sr_{2-x}Sm_x)FeMoO_6$ compounds, Physica B 405 (2010) 1428–1432.
[33] V. Ganeshchandra Prabhu, A.R. Paloly, N.G. Divya, M. Junaid Bushiri, Photocatalytic and ferromagnetic properties of electrically conducting multifunctional Ni/NiO nanocomposites in amorphous carbon matrix, Materials Science & Engineering B 228 (2018) 132–141.
[34] A.A. Al-Ghamdi, F. Al-Hazmi, R.M. Al-Tuwirqi, F. Alnowaiser, O.A. Al-Hartomy, F. El-Tantawyd, F. Yakuphanoglu, Synthesis, magnetic and ethanol gas sensing properties of semiconducting magnetite nanoparticles, Solid State Sci. 19 (2013) 111–116.